



CHORUS

This is the accepted manuscript made available via CHORUS. The article has been published as:

Anisotropy of electron and hole g tensors of quantum dots: An intuitive picture based on spin-correlated orbital currents

J. van Bree, A. Yu. Silov, M. L. van Maasakkers, C. E. Pryor, M. E. Flatté, and P. M.
Koenraad

Phys. Rev. B **93**, 035311 — Published 25 January 2016

DOI: [10.1103/PhysRevB.93.035311](https://doi.org/10.1103/PhysRevB.93.035311)

1 Anisotropy of electron and hole g tensors of quantum dots: an intuitive picture based 2 on spin-correlated orbital currents

3 J. van Bree,^{1,2,*} A. Yu. Silov,¹ M. L. van Maasakkers,¹ C. E. Pryor,² M. E. Flatté,^{1,2,†} and P. M. Koenraad¹

4 ¹*PSN, COBRA, University of Technology Eindhoven, 5600 MB Eindhoven, The Netherlands.*

5 ²*Department of Physics and Astronomy and Optical Science and Technology Center,*
6 *University of Iowa, Iowa City, Iowa 52242, USA*

7 (Dated: January 7, 2016)

Using single spins in semiconductor quantum dots as qubits requires full control over the spin state. As the g tensor provides the coupling in a Hamiltonian between a spin and an external magnetic field, a deeper understanding of the g tensor underlies magnetic field control of the spin. The g tensor is affected by the presence of spin-correlated orbital currents, of which the spatial structure has been recently clarified. Here we extend that framework to investigate the influence of the shape of quantum dots on the anisotropy of the electron g tensor. We find that the spin-correlated orbital currents form a simple current loop perpendicular to the magnetic moment's orientation. The current loop is therefore directly sensitive to the shape of the nanostructure: for cylindrical quantum dots the electron g tensor anisotropy is mainly governed by the aspect ratio of the dots. Through a systematic experimental study of the size dependence of the separate electron and hole g tensors of InAs/InP quantum dots, we have validated this picture. Moreover, we find that through size engineering it is possible to independently change the sign of the in-plane and growth direction electron g -factors. The hole g tensor is found to be strongly anisotropic, and very sensitive to the radius and elongation. The comparable importance of itinerant and localized currents to the hole g tensor complicates the analysis relative to the electron g tensor.

8 PACS numbers: 75.75.-c, 71.70.Ej, 73.21.La, 78.67.Hc

9 I. INTRODUCTION

10 The g tensor describes the fundamental coupling be-
11 tween a spin and an external magnetic field, and plays
12 therefore an essential role in the physics of spins. Ma-
13 nipulation of this tensor, for example by an electric field,
14 allows for an effective control over the spin even when an
15 externally applied magnetic field is static. This proves to
16 be advantageous for local addressing of spins^{1,2}, tilting
17 the spin's precessional axis³⁻⁷, or high-speed spin manip-
18 ulation⁸. Of particular interest is the g tensor of carri-
19 ers in (self-assembled) semiconductor quantum dots, as a
20 single spin inside these nanostructures is a promising can-
21 didate for forming a solid state qubit^{9,10}. Although the
22 electric-field sensitivity of the g tensor can be exploited as
23 a means to control the spin, it can also generate decoher-
24 ence when electrical (charge) noise is present¹¹. For op-
25 timal performance, control over the absolute value, sign,
26 and anisotropy of the g tensor is crucial. The effects of
27 quantum confinement and strain of the quantum dot are
28 usually captured by a parametrisation of the g tensor
29 in terms of size, shape and composition¹²⁻¹⁷. A better
30 understanding of the origin of the g tensor is therefore
31 helpful in the further exploration of electrical spin con-
32 trol.

33 The g tensor describes effectively how spin-orbit in-
34 teraction modifies the magnetic moment of a carrier. In
35 general the magnetic moment of a carrier can have con-
36 tributions from its spin and orbital degrees of freedom.
37 In the solid state the presence of spin-orbit interaction
38 and coupling between bands leads to a spin-correlated
39 orbital moment¹⁸. We will refer to this as just the or-

40 bital moment in this Article, noting that we mean the
41 spin-dependent orbital moment and not the conventional
42 orbital moment in absence of spin-orbit interaction. For
43 a conduction band electron in narrow-gap III-V semicon-
44 ductors, the orbital moment can be much larger than the
45 spin moment itself; the magnetic response of the electron
46 ground state spin is therefore dominated by the orbital
47 moment¹⁸. These orbital moments are generated through
48 orbital currents, of which the spatial structure in nanos-
49 tructures has been recently investigated¹⁹. The dominant
50 current was found to circulate within the nanostructure.
51 It vanishes at the edge and center and peaks about mid-
52 way between. This resembles a current loop, and this in-
53 tuitive physical picture is capable of explaining the size
54 and composition dependence of the spin-correlated or-
55 bital moment in various systems²⁰. Although the shape
56 of the nanostructure has been predicted to be of influence
57 on the electron g tensor^{12,13}, an intuitive picture of this
58 relation is still lacking. In Sec. II of this Article we will
59 show, using numerical $\mathbf{k} \cdot \mathbf{p}$ calculations and the intuitive
60 framework of orbital currents, how the anisotropy of the
61 electron g tensor is linked to the shape of a nanostruc-
62 ture.

63 Experimental efforts have been made to characterize
64 the g -factors (i.e. components of the g tensor) of exci-
65 tons²¹⁻²⁶, and of individual electron and holes²⁷⁻³⁶ con-
66 fined in quantum dots. Also electric control over g -factors
67 has been shown^{25,29,33,35-37}; in particular it was found
68 that the hole g -factor is much more sensitive to an electric
69 field than the electron g -factor. As quantum confinement
70 and strain affect the g tensor, it is generally found that
71 the inhomogeneous distribution of quantum dots leads to

72 different g -factors and electric-field sensitivities for each
 73 individually measured quantum dot. Although there are
 74 numerous reports of electron or hole g -factor measure-
 75 ments on individual quantum dots, there are only lim-
 76 ited systematic reports on the size dependence of the g -
 77 factors^{22–25}. Moreover, these only involve the exciton
 78 g -factor in a particular direction, and therefore do not
 79 reveal the size dependence of the separate electron and
 80 hole g tensors and their anisotropies.

81 In Sec. III of this Article we report a systematic ex-
 82 perimental study of the size dependence of the separate
 83 electron and hole g -factors of InAs/InP quantum dots
 84 in both the growth and in-plane direction. It provides
 85 insight in the possibility to size engineer the magnitude
 86 and sign of components of the g tensor. Moreover, it
 87 allows us to verify the correlation motivated by the the-
 88 ory in Sec. II between the nanostructure’s shape and the
 89 anisotropy of the electron g tensor. We have measured
 90 the separate electron and hole g tensors using angle-
 91 dependent magnetoluminescence (Sec. III A). Contrary
 92 to what has been found before^{30,31,35,36}, we have system-
 93 atically measured a strong electron g -factor anisotropy
 94 (Sec. III B). Through the systematic study of the size
 95 dependence, we have been able to understand this be-
 96 haviour and find it in good agreement with our theo-
 97 retical predictions. The experimentally measured hole g -
 98 factors (Sec. III C) agree well with numerical calculations.
 99 Also the exciton diamagnetic coefficients (Sec. III D) are
 100 found to be anisotropic; analogous to the electron g ten-
 101 sor, this anisotropy can be correlated with the shape of
 102 the quantum dots.

103 II. THEORY OF SPIN-CORRELATED ORBITAL 104 MOMENTS IN ANISOTROPIC DOTS

105 Calculations using analytical perturbation theory¹²
 106 and numerical methods¹³ have predicted that the shape
 107 of the nanostructure influences the anisotropy of the elec-
 108 tron g tensor. However, an intuitive explanation of this
 109 relation is lacking. We therefore investigate how the or-
 110 bitral currents change when the spin of a carrier is oriented
 111 in different directions. Intuitively one would expect the
 112 orbital current to circulate in a plane perpendicular to
 113 the orbital moment. To verify this intuition, we calcu-
 114 late explicitly the orbital current density of cylindrical
 115 InAs/InP quantum dots.

116 We compute the electron ground state using strain-
 117 dependent eight-band $\mathbf{k}\cdot\mathbf{p}$ -theory in the envelope approx-
 118 imation with finite differences on a real space grid^{38–40}.
 119 The strain is calculated using linear elasticity continuum
 120 theory. The calculations are performed at $T = 0$ K and
 121 material parameters are taken from Ref. 41. The mag-
 122 netic field is included by coupling it to both the spin part
 123 (using the Zeeman Hamiltonian) and the orbital part (us-
 124 ing the gauge-invariance) of the wave function^{13,14}. Using
 125 a small magnetic field of 0.1 T, the electron ground state’s
 126 magnetic moment is oriented an angle η away from the

127 symmetry z -axis of the quantum dot towards the in-plane
 128 x -axis.

129 Knowing the real-space wave function of this oriented
 130 electron ground state, we can calculate the orbital cur-
 131 rent using the formalism developed in Ref. 19. We use
 132 an envelope-function formalism to describe the electronic
 133 state, where the wave function is the sum of products
 134 of a (slowly-varying) envelope function and a (quickly-
 135 varying) Bloch function. When evaluating the spatial
 136 dependence of the current associated with that state we
 137 evaluate the current operator, which is directly related to
 138 the spatial derivative operator. As a result the derivative
 139 of the Bloch function dominates the current¹⁹. The or-
 140 bitral current can be generally decomposed into localized
 141 currents, which are restricted to a unit cell, and itiner-
 142 ant currents, which are distributed throughout the quan-
 143 tum dot. Since the electron ground state mainly consists
 144 of conduction band states which carry no Bloch orbital
 145 moment, the localized currents have a negligible contri-
 146 bution to the total current. The dominant contribution
 147 to the orbital current comes therefore from the itinerant
 148 currents related to the Bloch velocity. For more details
 149 see Refs. 19 and 20.

150 In Fig. 1(a) we show selected streamlines of this dom-
 151 inant orbital current density for three differently sized
 152 quantum dots at three different values of η . We con-
 153 firm the previous finding that the current is zero at the
 154 center and edge of the quantum dot, and peaks some-
 155 where in between. We also observe that for $\eta \neq 0^\circ$ the
 156 current density is not uniform along a streamline, which
 157 originates from the divergence-free nature of the current
 158 density. More importantly, however, we indeed observe
 159 that the current circulates in a plane perpendicular to the
 160 magnetic moment. The orbital moment is thus generated
 161 from a current loop perpendicular to its orientation.

162 This finding has an interesting consequence. The mag-
 163 nitude of an orbital moment μ_{orb} depends on the area A
 164 the integrated current I encircles, $\mu_{\text{orb}} = IA$. The or-
 165 bitral moment is therefore sensitive to the shape of the
 166 quantum dot through the area its generating current en-
 167 circles. In particular, we expect for cylindrically shaped
 168 quantum dots with radius R and height H

$$\mu_{\text{orb}}^z \propto R^2, \quad \mu_{\text{orb}}^x \propto \frac{1}{2}RH = \frac{R^2}{\lambda},$$

169 where we used the aspect ratio $\lambda = 2R/H$.

170 We find indeed that the orbital moment follows this ex-
 171 pectation, see Fig. 1(b). The orbital moment of the quan-
 172 tum dot with near unity aspect ratio is isotropic, while for
 173 large (small) aspect ratios we observe that μ_{orb}^x smaller
 174 (larger) than μ_{orb}^z . We point out that the anisotropy
 175 has significant magnitude; in this example $> 15\%$ of the
 176 orbital moment itself. Only orbital currents that are
 177 distributed throughout the quantum dot will sense the
 178 shape of the nanostructure. Other contributions¹⁹ to the
 179 total magnetic moment (notably the spin moment) arise
 180 mostly from small localized currents, and do indeed not

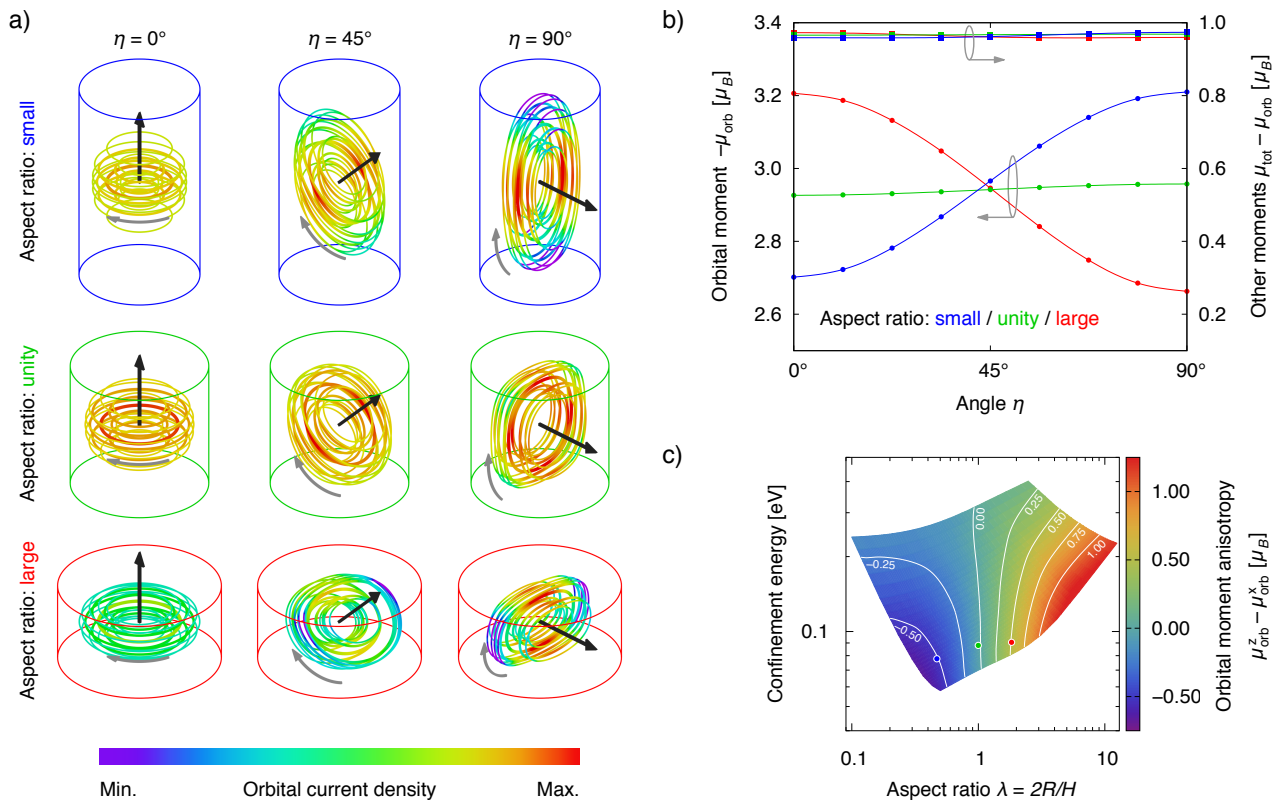


FIG. 1. (a) Selected streamlines of the (itinerant Bloch velocity related) orbital current density of the electron ground state of three different cylindrical InAs/InP quantum dots for three different angles η . The current circulates (grey arrow) in a plane perpendicular to the orbital moment (black arrow). (b) The orbital moment for the three quantum dots of (a) as function of the polar angle η . The pronounced anisotropy is only present for the orbital moment, not for the other contributions to the total magnetic moment. (c) The orbital moment anisotropy depends strongly on the aspect ratio λ and relatively weakly on the confinement energy, from which it is inferred that the anisotropy is governed mainly by the shape of the nanostructure. The three coloured dots indicate the three quantum dots shown in (a) and (b).

181 exhibit a significant anisotropy, see Fig. 1(b). The orbital 198
 182 moment also depends through the integrated current I on
 183 the geometry of the nanostructure.

184 To investigate whether the anisotropy is truly governed 204
 185 by the shape of the quantum dot, we show in Fig. 1(c) 205
 186 how the anisotropy depends on the aspect ratio and the 206
 187 confinement energy. The strong dependence on the aspect 207
 188 ratio indicates directly that the anisotropy is driven 208
 189 by the nanostructure's shape. Simultaneously we observe 209
 190 only a weak dependence of the anisotropy on the confine- 210
 191 ment energy. For a fixed aspect ratio we expect the confine- 211
 192 ment energy to depend only on the volume, and we 212
 193 therefore infer that the anisotropy is relatively insensitive 213
 194 to the overall size of the nanostructure. This relation is 214
 195 also showcased by the three quantum dots exemplified in 215
 196 Fig. 1(a) and (b): they have nearly the same confinement 216
 197 energy, yet very different orbital moment anisotropies. 217

III. EXPERIMENTAL RESULTS

199 To experimentally verify whether the orbital moment
 200 anisotropy is indeed linked to the shape of nanostruc-
 201 tures, we have measured the g tensor of individual
 202 InAs/InP quantum dots. We have studied these quantum
 203 dots in the past and summarize here for reference some of
 204 our previous findings²⁴. These quantum dots were grown
 205 by metal-organic vapor-phase epitaxy, resulting in a in-
 206 homogeneous size distribution and a broad emission en-
 207 ergy range. The ensemble photoluminescence spectrum
 208 contained multiple peaks, which we interpreted as a mul-
 209 timodal height distribution. This implied that the emis-
 210 sion energy of these quantum dots is strongly correlated
 211 with their height. We have measured the heights of more
 212 than 50 dots using cross-sectional scanning tunnelling
 213 microscopy (X-STM) to independently verify this inter-
 214 pretation. The resulting distribution showed that the
 215 heights vary between 5 and 15 monolayers (1.5–4.5 nm),
 216 matching well with the peaks found in the ensemble
 217 photoluminescence. The X-STM measurements also

revealed that the quantum dots resemble best cylindrical disk. The lateral size of the quantum dots was found to be less well defined; the largest radius measured 15 nm. These quantum dots have therefore a large aspect ratio and provide a good test ground for our predicted electron g tensor anisotropy.

The g tensor \mathbf{g} of our quantum dots is diagonal due to their approximate D_{2d} symmetry. We can relate the g -factors appearing on the diagonal of the g tensor to the orbital moment via $g^{x,y,z} = 2/\mu_B(\mu_{\text{spin}}^{x,y,z} + \mu_{\text{orb}}^{x,y,z})$. Here $\mu_{\text{spin}}^{x,y,z}$ is the spin moment, $\mu_{\text{orb}}^{x,y,z}$ the orbital moment, and μ_B the Bohr magneton. We note that this relation can be derived using the Zeeman interaction and time-reversal symmetry; the factor 2 arises from Kramer's degeneracy. It has been shown²⁰ that μ_{spin}^z is nearly always equal to μ_B . In Fig. 1(b) we have also shown that the spin moment does not exhibit any significant anisotropy. It is therefore a good approximation to set $\mu_{\text{spin}}^{x,y,z} = \mu_B$. Measuring a g -factor determines therefore effectively the orbital moment in that direction.

A. Experimental methods

The electron and hole ground states of our quantum dots are doubly degenerate at zero magnetic field due to their approximate D_{2d} symmetry (neglecting Coulomb and exchange effects)²¹. A magnetic field lifts this spin degeneracy, which results in four possible optical transitions between the eigenstates of the Zeeman Hamiltonian⁴². Both the electron and hole spin can be effectively described⁴³ as a spin $s_{e,h} = \frac{1}{2}$, since the hole state has a strong heavy-hole (HH) character due to quantum confinement and strain¹⁶. The Zeeman Hamiltonian has then the same form for the electron (e) and hole (h)

$$\begin{aligned} \mathcal{H}_{\text{Zeeman}}^{e,h} &= \mu_B \mathbf{B} \cdot \mathbf{g}_{e,h} \cdot \mathbf{s}_{e,h} \\ &= \frac{1}{2} \mu_B B \begin{pmatrix} g_{e,h}^z \cos \eta & g_{e,h}^x \sin \eta \\ g_{e,h}^x \sin \eta & -g_{e,h}^z \cos \eta \end{pmatrix}, \quad (1) \end{aligned}$$

where $\mathbf{s}_{e,h} = \frac{1}{2}(\sigma_x, \sigma_y, \sigma_z)$ the spin operator, $\mathbf{B} = (B \sin \eta, 0, B \cos \eta)$ the magnetic field as defined in Fig. 2(a), and $\mathbf{g}_{e,h}$ the g tensor. Since light-matter interaction conserves spin, it follows from Eq. 1 that for $\eta = 0^\circ$ (Faraday geometry) only two of the four transitions are optically addressable, from which only $g_e^z + g_h^z$ can be determined. All four transitions are visible when $\eta \neq 0^\circ$. A measurement at $\eta = 90^\circ$ (Voigt geometry) determines separately g_e^x and g_h^x . To separate g_e^z and g_h^z , it is customary^{30,31,42} to do an additional measurement at an intermediate angle ($\eta = 45^\circ$).

Following this approach, we have investigated the photoluminescence as function of a magnetic field up to 10 T at 4 K of 55 individual quantum dots in the same sample used in Ref.²⁴. We used a small periscope arrangement of four right-angle mirrors to vary the angle η , see Fig. 2(a). We have used an Al mask with apertures in

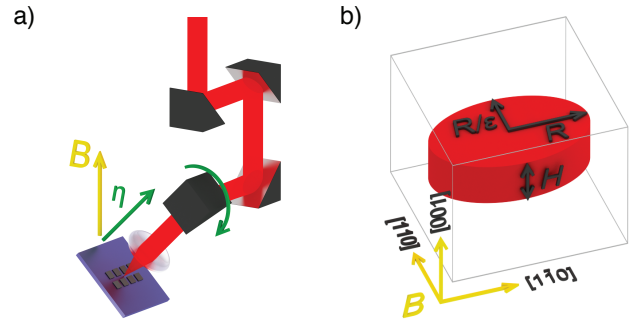


FIG. 2. (a) An ex-situ rotatable periscope has been used to change the angle η between the magnetic field (yellow) and the sample's normal (green). (b) Calculations have been performed on InAs cylindrical disks (red) embedded in InP with radius R and height H ; for some calculations the radius in the $[110]$ -direction is compressed by ϵ ; magnetic fields have been applied in the indicated directions.

order to systematically relocate the same quantum dot after changing η ex-situ. Photo-excitation is provided by a cw 635 nm laser diode; the photoluminescence is collected in backscattering geometry and analysed using a single grating spectrometer and liquid nitrogen cooled InGaAs linear array detector. The spectra are fitted to obtain the peak positions of an individual quantum dot with an accuracy of less than 50 μeV .

In Fig. 3(a) we show the magnetoluminescence of an individual quantum dot up to 10 T for $\eta = (0^\circ, 45^\circ, 90^\circ)$. The polarisation of the luminescence is determined at 10 T and is found to be circular (σ^\pm) for $\eta = 0^\circ$ and linear ($\pi_{x,y}$) for $\eta = 90^\circ$. From the fitted peak positions we obtain the Zeeman energy, see Fig. 3(b). The g tensor can be extracted from these Zeeman energies by fitting them with the transitions energies (which follow from diagonalization of Eq. 1):

$$\begin{aligned} E^{\xi_e, \xi_h} &= E_0 + \mu_B \left[\xi_e \sqrt{(g_e^x \sin \eta)^2 + (g_e^z \cos \eta)^2} \right. \\ &\quad \left. + \xi_h \sqrt{(g_h^x \sin \eta)^2 + (g_h^z \cos \eta)^2} \right] |B| \\ &\quad + (\alpha^z \cos^2 \eta + \alpha^x \sin^2 \eta) B^2 \quad (2) \end{aligned}$$

where $\xi_{e,h} = (+, -)$ depending on the electron or hole spin orientation, and E_0 is the transition energy at zero magnetic field. We added the η -dependence of the diamagnetic shift using the diamagnetic coefficients at $\eta = 0^\circ$ (α^z) and $\eta = 90^\circ$ (α^x). The Zeeman energies at all values of η are fitted simultaneously with Eq. 2, see Figs. 3(b) and (c). Using this procedure, we have extracted the g -factors and diamagnetic coefficients for 55 individual quantum dots having different emission energies E_0 , which we will discuss in Secs. III B - III D. We refer the reader to the Appendix for a detailed discussion on the assumptions made in the fitting procedure; these influence the assignment and sign of the various g -factors.

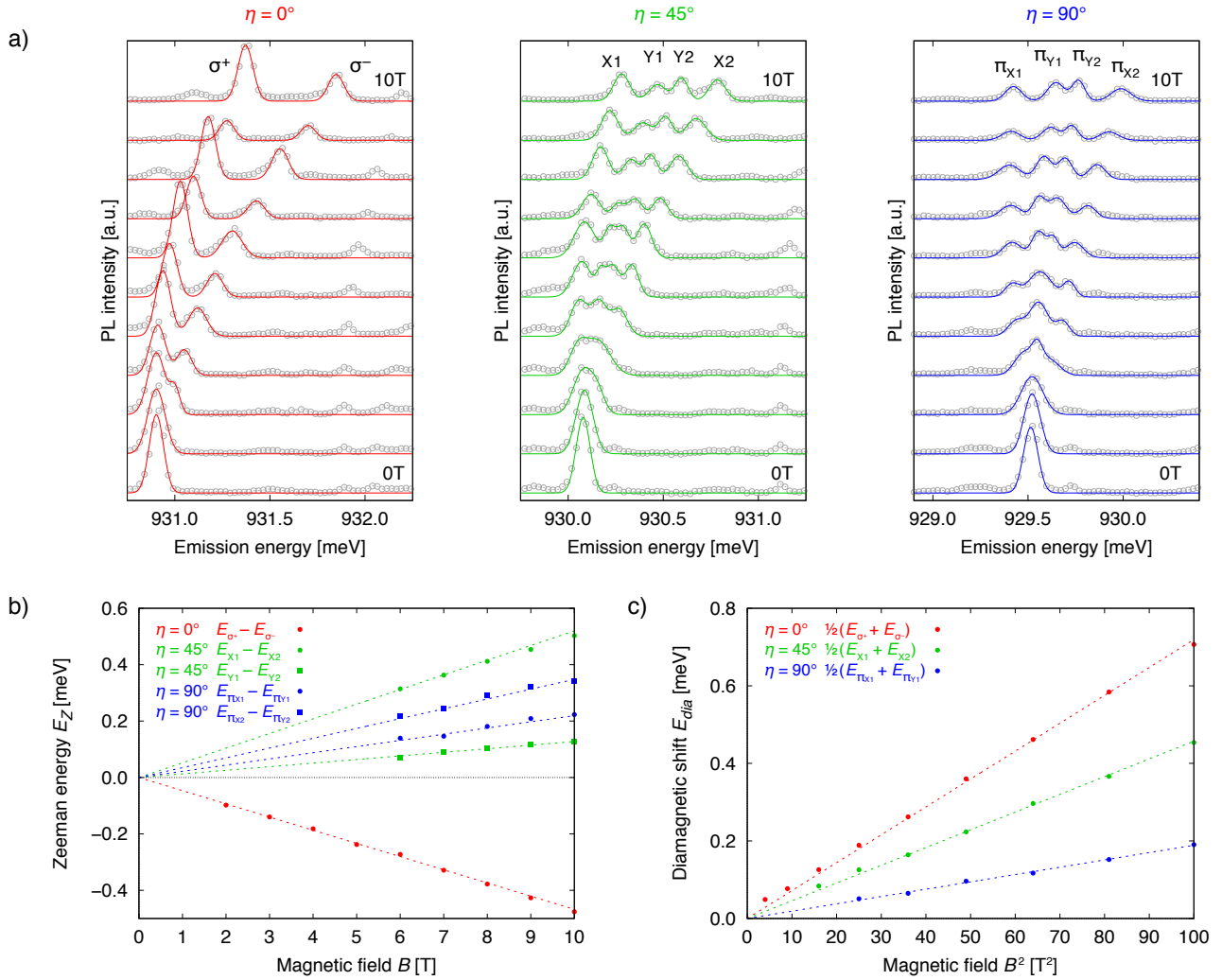


FIG. 3. (a) An example of the magnetoluminescence up to 10 T of a single quantum dot for $\eta = 0^\circ$, $\eta = 45^\circ$, and $\eta = 90^\circ$. The experimental data (gray points) and the fits (colored lines) are offset for clarity for increasing magnetic field. We obtain from the fitted peak positions the Zeeman energies (b) and diamagnetic shifts (c). By simultaneous fitting of these energies using Eq. 2, we find for this particular quantum dot ($g_e^x = 0.60$, $g_e^z = -0.51$, $g_h^x = 0.38$, $g_h^z = -0.29$) and ($\alpha^z = 7.2 \mu\text{eV}/\text{T}^2$, $\alpha^{45^\circ} = 4.6 \mu\text{eV}/\text{T}^2$, $\alpha^x = 1.9 \mu\text{eV}/\text{T}^2$).

297 To understand the origin and size dependence of the
 298 experimentally measured g -factors in detail, we calcu-
 299 lated the g -factors using the same $\mathbf{k} \cdot \mathbf{p}$ -model used in
 300 Sec. II. The quantum dots are modelled as pure InAs
 301 disks embedded in InP, see Fig. 2(b). The separate elec-
 302 tron and hole energy levels of a quantum dot have been
 303 calculated as function of a magnetic field applied in the
 304 growth [001]-direction or in-plane $\langle 110 \rangle$ -directions. We
 305 can then directly extract from these energy levels the Zee-
 306 man energy ($g_{e,h}^{x,z}$ -factors) and diamagnetic shift ($\alpha_{e,h}^{x,z}$).
 307 Both the size of the quantum dot and elongation of its
 308 footprint $\varepsilon = R_{[1\bar{1}0]}/R_{[110]}$ have been varied. We have left
 309 out the remote-band coupling of the hole spin to the mag-
 310 netic field in all calculations, as previous work indicated
 311 this is a better approximation than including them¹⁶.

B. Electron g -factors

313 From Fig. 4 we see that the measured electron g -factors
 314 are strongly correlated with the emission energy. As the
 315 emission energy is strongly determined by the height of
 316 the quantum dots²⁴, these trends can therefore be in-
 317 terpreted as the height dependence of the g -factor. A
 318 comparison between the trends of the experimental data
 319 and the calculated electron g -factors confirms this con-
 320 clusion. We simultaneously conclude that all quantum
 321 dots have more or less the same radius, which agrees well
 322 with the observation that the diamagnetic coefficients do
 323 not depend much on the emission energy (see Sec. III D).
 324 A radius between 7 and 11 nm and a height between 1.8
 325 and 6.0 nm gives the best match between experiment and

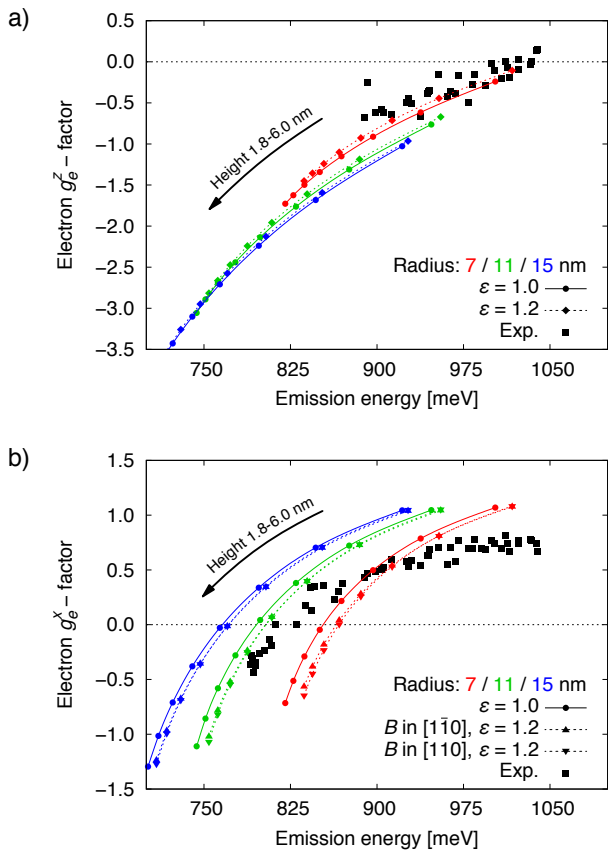


FIG. 4. The experimentally measured (black squares, $\Delta g = 0.1$) and calculated (coloured curves) electron g_e^z (a) and g_e^x -factors (b) as function of the emission energy of the quantum dot. The different colours indicate different radii of the disks; the height is varied from 1.8 – 6.0 nm along a curve of fixed radius. The continuous lines are cylindrical disks, the dotted curves for an elongated disk with $\epsilon = 1.2$. In the latter case, the in-plane orientation of the magnetic field ($[110]$ upward triangles, $[1\bar{1}0]$ downward triangles) affects the calculated g_e^x -factors.

calculations. This agrees well with the average height of 3 nm and maximum radius of 15 nm determined by X-STM²⁴. We would like to stress that the calculations with the $\mathbf{k} \cdot \mathbf{p}$ -model are fit-free and completely independent from the experimental results. We attribute deviations between the experimental and calculated g -factors to differences between the real and modelled shape, size and composition of the quantum dots.

Recently InAs/In_{0.53}Al_{0.24}Ga_{0.23} quantum dots, which also emit around 800 meV, have been investigated⁴⁴. Although these quantum dots have a confinement energy comparable to our quantum dots, their average size (radius of 25 nm and height of 13 nm) and composition differ substantially. Based on the framework of the orbital currents, we would expect the larger size of the InAs/In_{0.53}Al_{0.24}Ga_{0.23} to result into a larger orbital moment. Indeed, g_e^x was measured to be about -1.9 , which is more negative than our measurements. It shows that

a g -factor is more affected by the size of a quantum dot than by its confinement energy.

A more prominent experimental observation can be made by comparing Figs. 4(a) and (b): for each quantum dot g_e^x is significantly closer to the free electron value of $+2$ than g_e^z . Translated in terms of the orbital moment: for every quantum dots we observe $\mu_{\text{orb}}^x < \mu_{\text{orb}}^z$. This complies with our theoretical prediction: as these cylindrical quantum dots have a large aspect ratio, the orbital current can encircle a much larger area when the orbital moment is along the symmetry axis than when it is directed in-plane. Although the anisotropy of the electron g -factor has been experimentally measured before in quantum wells⁴⁵ and quantum dots^{29-31,35-37}, the reported anisotropies have been generally small and were not explained using this simple geometrical argument. We point out that the anisotropy makes it possible to size engineer separately g_e^x and g_e^z close to zero, where an additional electric field can then be used to change the sign of the g -factor.

The behavior of electron g tensors is sometimes explained using 'averaging methods': the penetration of the state into the barriers determines, through the difference of the bulk g -factors of the nanostructure and barrier material, the value of the g -factor. Interestingly, the averaging method would predict an isotropic electron g tensor, since the penetration into the barrier material is independent of the spin orientation (neglecting the very small anisotropy of the bulk g tensor). Although the shortcomings of this approach have been pointed out before^{13,16}, our experimentally observed strong anisotropy of the electron g tensor invalidates this type of approach.

The geometrical argument complies well with some details in the size-dependence of the calculated g -factors. Firstly, we observe in Fig. 4 that for a fixed height the radius has a much larger influence on g_e^z (sensitive to R^2) than on the g_e^x (sensitive to $RH/2$). In particular, we see that for very flat quantum dots the radius has very little influence on g_e^x and affects only the emission energy. Secondly, we see that elongation slightly decreases μ_{orb}^z , since it limits the total area for the current to circulate. Simultaneously we observe that elongation does not have a great effect on μ_{orb}^x , as the area for the current to circulate in is mainly limited by the height. Lastly, we see that μ_{orb}^x is largest if the magnetic field is along the $[110]$ -direction, since the area for the current to circulate in is now enlarged by the elongation.

The prominent height dependence of g_e^z cannot be intuitively explained using the geometrical argument. This dependence is therefore related to the size dependence of the integrated current²⁰. For the small heights considered here, the integrated current gets smaller with decreasing height: the valence band contributions to the electron ground state are quenched through their dependence on the confinement energy. This explains why the calculated curves for different radii are more or less falling on top of each other: g_e^z is mainly parameterized by the confinement energy. The confinement energy scales with

402 the volume of the quantum dot for a fixed aspect ratio.
 403 The g_e^z -factor depends therefore mostly on the volume,
 404 as was found before¹³.

405 C. Hole g -factors

406 From Fig. 5(a) and (b) we observe that the experimen-
 407 tally found g_h^x and g_h^z are very different: the hole g tensor
 408 is an even more anisotropic than the electron g tensor.
 409 Contrary to the electrons, the strong (weak) correlation
 410 of g_h^z (g_h^x) with emission energy makes it possible to size
 411 engineer the hole g tensor to become isotropic. More-
 412 over, the sign of the g_h^z -factors changes around 900 meV,
 413 which can be beneficial for applications.

414 To explain this behaviour we need to trace the origin
 415 of the orbital moment of the hole ground state. As a first
 416 approximation, the hole state is a pure HH state. Such
 417 state has, in addition to its spin moment, only a localized
 418 Bloch orbital moment that is projected along the z -axis:
 419 we would therefore expect $g_h^x = 0$ and $g_h^z = +4$. From
 420 Fig. 5(a) and (b) we see that this expectation is not far
 421 off for g_h^x , but the both the experimental and calculated
 422 g_h^z behave very differently. This points to the more com-
 423 plicated nature of the hole orbital moment compared to
 424 the electron orbital moment. In general, contributions
 425 from other bands lead to additional localized and itiner-
 426 ant orbital currents. For the electron state it turns out
 427 that the itinerant current dominates all other contribu-
 428 tions¹⁹, such that it solemnly explains the experimen-
 429 tally observed trends as we have shown in Sec. III B. For
 430 the hole state however, both types of currents contribute
 431 equally, thereby complicating the analysis.

432 To make progress, we can semi-quantitatively investi-
 433 gate the first and most important contribution to the hole
 434 state: the light-hole (LH) band. In Fig. 5(c) we show the
 435 LH-contribution of the calculated hole ground state for
 436 the same sizes of quantum dots as in Fig. 5(a) and (b).
 437 We observe that the LH-contribution increases with in-
 438 creasing height, decreasing radius and increasing elonga-
 439 tion. This behaviour can be understood by inspecting
 440 the part of the eight-band Hamiltonian describing the
 441 Γ_8^v -bands⁴⁶:

$$\mathcal{H}_{\Gamma_8^v} = \begin{pmatrix} E_{\text{HH}} & L & M & 0 \\ L^* & E_{\text{LH}} & 0 & M \\ M^* & 0 & E_{\text{LH}} & -L \\ 0 & M^* & -L^* & E_{\text{HH}} \end{pmatrix} \quad (3)$$

442 where

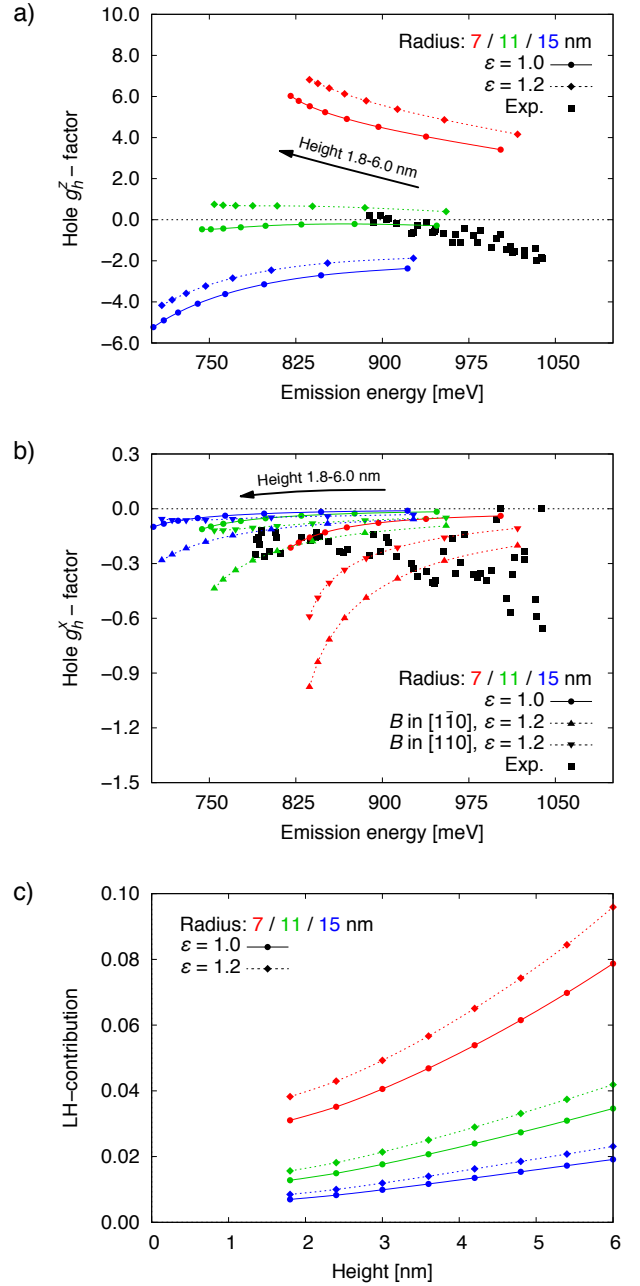


FIG. 5. The experimentally measured (black squares, $\Delta g = 0.1$) and calculated (coloured curves) hole g_h^z (a) and g_h^x (b) as function of the emission energy of the quantum dot. The different colours indicate different radii of the disks; the height is varied from 1.8 – 6.0 nm along a curve of fixed radius. The continuous lines are cylindrical disks, the dotted curves for an elongated disk with $\epsilon = 1.2$. In the latter case, the in-plane orientation of the magnetic field ($[110]$ upward triangles, $[1\bar{1}0]$ downward triangles) affects the calculated g_h^x -factors. (c) The LH-contribution to the calculated hole ground state for different height and radii of the quantum dots.

$$E_{\text{HH}} = -\frac{\hbar^2 (k_x^2 + k_y^2)}{2m_0}(\gamma_1 + \gamma_2) - \frac{\hbar^2 k_z^2}{2m_0}(\gamma_1 - 2\gamma_2) \quad (4)$$

$$E_{\text{LH}} = -\frac{\hbar^2 (k_x^2 + k_y^2)}{2m_0}(\gamma_1 - \gamma_2) - \frac{\hbar^2 k_z^2}{2m_0}(\gamma_1 + 2\gamma_2) \quad (5)$$

$$L = \sqrt{3} \frac{\hbar^2 (k_x - ik_y) k_z}{m_0} \gamma_3 \quad (6)$$

$$M = \sqrt{3} \frac{\hbar^2 (k_x - ik_y)^2}{2m_0} \gamma_3 \quad (7)$$

443 where $k_{x,y} \sim 1/R$ and $k_z \sim 1/H$ are the wave numbers
 444 of the state⁴⁷, and $\gamma_{1,2,3}$ are the Luttinger parameters.
 445 In the framework of perturbation theory, the amount of
 446 LH-contribution in the hole state is proportional to the
 447 coupling between the HH and LH bands (matrix elements
 448 L and M) divided by the energetic splitting between the
 449 bands ($E_{\text{HH}} - E_{\text{LH}}$). As for our quantum dots $H \ll R$,
 450 we immediately infer that the hole state is predominantly
 451 HH in character. Moreover, we see that increasing the
 452 height (radius), the energetic splitting $E_{\text{HH}} - E_{\text{LH}}$ be-
 453 comes smaller (larger) and hence the LH-contribution
 454 larger (smaller), like we observe in Fig. 5(c). Also the
 455 increase of the LH-contribution with elongation can be
 456 explained, since the coupling terms L and M are propor-
 457 tional to $k_x - k_y \propto \varepsilon$.

458 Comparing Fig. 5(b) and (c) we observe a positive corre-
 459 lation between the LH-contribution and the magnitude
 460 of the calculated g_h^x -factors. Elongation also increases the
 461 calculated g_h^x and has a more profound influence than the
 462 LH-contribution, pointing out that elongation affects g_h^x
 463 also via other bands. The large spread of the measured
 464 g_h^x at high emission energy can therefore be attributed
 465 to a larger LH-contribution or elongation. In previous
 466 experiments, we found about 20% of our quantum dots
 467 to exhibit an anisotropic exchange splitting at zero mag-
 468 netic field²⁴. Since this splitting increased towards higher
 469 emission energies, we tentatively argued that the elon-
 470 gation is more pronounced at higher emission energies.
 471 Such an effect could explain the experimentally observed
 472 increase of g_h^x at large emission energies.

473 Both the measured and calculated g_h^z show a clear
 474 trend with emission energy. The calculated g_h^z also de-
 475 pends strongly on the radius, which could be related to
 476 the area ($\propto R^2$) in which the itinerant orbital current
 477 circulates. Also the integrated current I itself might de-
 478 pend directly on the radius through the size dependence
 479 of the contributions of other bands. The combined effect
 480 might explain the unexpected strong radius dependence
 481 of the calculated g_h^z -factors. We again point out that also
 482 the localized orbital currents might play a significant role
 483 here.

484 D. Diamagnetic coefficients

485 An external magnetic field induces through the Lorentz
 486 force an orbital current for carriers confined in quantum

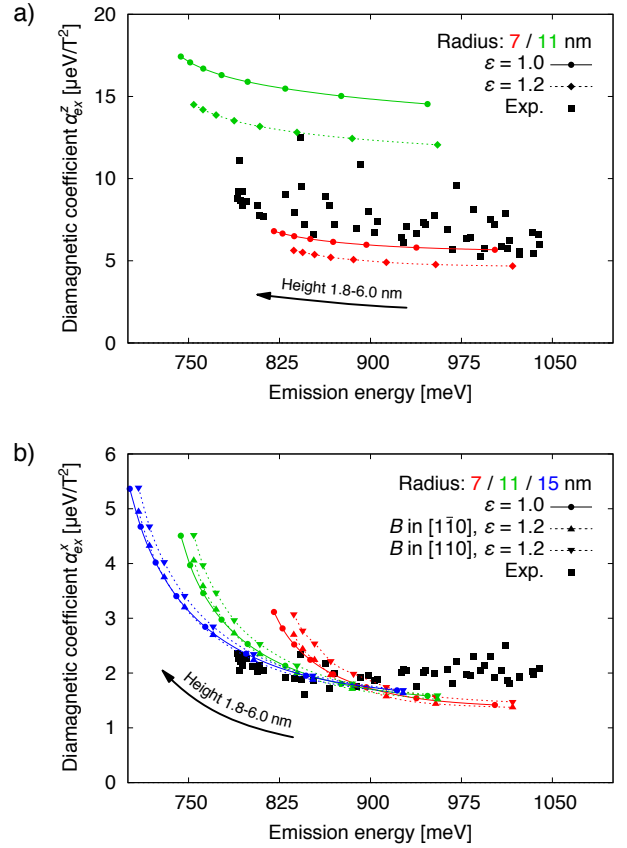


FIG. 6. The experimentally measured (black squares) and calculated (coloured curves) exciton diamagnetic coefficients α_{ex}^z (a) and α_{ex}^x (b) as function of the emission energy of the quantum dot. The different colours indicate different radii of the disks; the height is varied from 1.8 – 6.0 nm along a curve of fixed radius. The continuous lines are cylindrical disks, the dotted curves for an elongated disk with $\varepsilon = 1.2$. In the latter case, the in-plane orientation of the magnetic field ([110] upward triangles, $[1\bar{1}0]$ downward triangles) affects the calculated diamagnetic coefficients.

487 dots, analogous to Langevin diamagnetism in atoms. In
 488 contrast to the spin-correlated currents underlying the
 489 g tensor, this magnetic field induced current is spin-
 490 independent. For a magnetic field along the z -axis, an
 491 elementary derivation shows that this leads to a diamag-
 492 netic shift in energy

$$\mu_{dia} = IA = \left(\frac{-e\omega}{2\pi} \right) \pi R^2 \rightarrow E_{dia} = -\mu_{dia} B = \frac{e^2 R^2}{4m^*} B^2 \quad (8)$$

where $\omega = eB/2m^*$ due to Larmor precession, and m^* is the effective mass. The factor in front of the B^2 -dependence is defined as diamagnetic coefficient α . In analogy with the spin-correlated currents (Sec. II) we

therefore intuitively expect

$$\alpha^z \propto \frac{R^2}{m_z^*(R, H)}, \quad \alpha^x \propto \frac{RH}{m_x^*(R, H)}. \quad (9)$$

Similar to the anisotropy of the electron g tensor, the diamagnetic energy anisotropy is sensitive to the shape of the quantum dot through the area the magnetic field induced current encircles. Note that it also depends through the effective mass anisotropy on the size of the quantum dots.

Experimentally we measure the exciton diamagnetic coefficients α_{ex} , which contain the combined electron and hole diamagnetic coefficients. We still expect that the anisotropy of α_{ex} is largely determined by the aspect ratio, since the hole effective mass is much larger than the electron effective mass. It is therefore possible to approximately infer from the anisotropy of α_{ex} what aspect ratio the nanostructures have. We find from the measurements shown in Fig. 6 that $\alpha_{ex}^z/\alpha_{ex}^x = (3.7 \pm 0.9)$, meaning that our quantum dots are indeed flat disks. Moreover, the ratio's weak dependence on the emission energy indicates that all quantum dots have a similar aspect ratio. This independently validates the results of the structural analysis²⁴ and the assertions made in the discussion on the g tensors.

The α_{ex}^z , see Fig. 6(a), are similar to the previously reported exciton diamagnetic coefficients²⁴. The weak dependence on the emission energy indicates that the measured quantum dots have similar radii. This complies well with the comparison between the measured and calculated electron g -factors: also there we found that a single radius gives the best match. We find again that a radius between 7 and 11 nm gives the best match between experiment and calculations; this can be improved further by including Coulomb corrections¹⁶. As expected, the theoretically calculated α_{ex}^z depend strongly on the radius and the elongation, as both influence the area the magnetic-field induced orbital current circulates. Their less-intuitive height dependence was previously found to be related to the size (or energy) dependence of the effective mass¹⁶.

The α_{ex}^x , see Fig. 6(b), has not been previously measured systematically at different emission energies. There is good agreement between the experimentally observed and calculated α_{ex}^x ; the deviation at larger emission energies could be related to the discrepancy found for the g_h^x -factors at those energies. The calculated α_{ex}^x depend relatively more strongly on the height than the α_{ex}^z : this complies with our expectation that α_{ex}^x is directly proportional to the height. Indeed we find from our calculations that the separate electron and hole diamagnetic coefficients are (approximately) linearly dependent on both height and radius (not shown here).

IV. CONCLUSIONS

We have predicted that the anisotropy of the electron g tensor is strongly correlated with the shape of the nanostructure in a fashion traceable to the behavior of the spin-correlated orbital currents. The orbital current that generates the spin-correlated electron orbital moment circulates in a plane perpendicular to the moment's orientation. The resulting simple current loop is therefore sensitive to the shape of the nanostructure. For cylindrical quantum dots this results in the an anisotropic electron g tensor, which is governed mainly by the aspect ratio of the quantum dots. Through a systematic study of the size dependence of the separate electron and hole g tensors of flat quantum dots, we have verified that this picture is valid. Moreover, the experimentally observed anisotropy directly invalidates 'averaging methods' for calculating g -factors.

We find that through size-engineering it is possible to independently change the sign of the in-plane and growth direction electron g -factors. The influence of elongation follows the intuitive picture of the simple current loop, and is of small influence for the electron g tensor. The hole g tensor is strongly anisotropic, and very sensitive to the radius and elongation. Although the underlying hole orbital moment can be partially understood from the LH-contribution, the equal importance of both itinerant and localized currents complicates the analysis over the electron case.

The approximate analogous role of circulating currents on the diamagnetic coefficients and g tensors, means that the shape of nanostructures also determine the anisotropy of the diamagnetic coefficients. It is therefore possible to infer from the anisotropy of the diamagnetic coefficients what aspect ratio nanostructures have.

M.E.F. acknowledges support from an AFOSR MURI. J. v. B., A. Yu. S., and P. M. K. acknowledge support by the COBRA Research Institute.

Appendix: Comments on assignment, sign, and detection range of g -factors

As can be seen from Eq. 2, only the absolute value of the g -factors are relevant for determining the energy levels in the $\eta = 45^\circ$ geometry. Therefore the sign of $g_{e,h}^z$ ($g_{e,h}^x$) is solely determined by the $\eta = 0^\circ$ ($\eta = 90^\circ$) measurements. In the Faraday measurements, the circular polarisation state of the light leads directly to the sign of the exciton g_{ex}^z -factor:

$$g_{ex}^z = \frac{E_{\sigma^+} - E_{\sigma^-}}{\mu_B B} = g_e^z + g_h^z \quad (A.1)$$

which complies with the usual definitions^{14,24}. As in our measurements $g_{ex}^z \neq 0$, this relation determines directly the sign of the separate electron and hole g^z -factors.

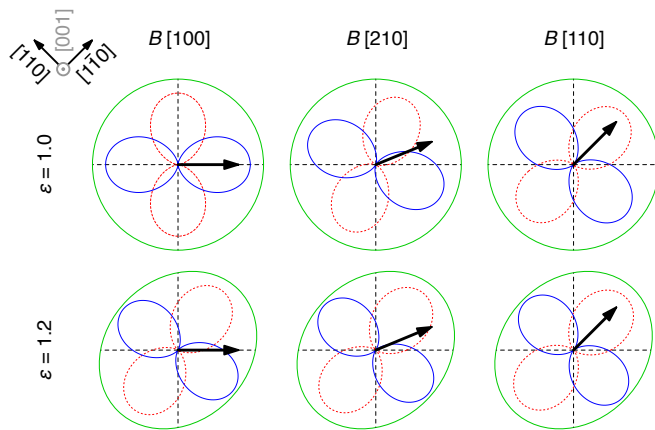


FIG. 7. The calculated linear polarisation pattern (blue/red) for emission along the z -axis when the in-plane magnetic field is rotated from the $[100]$ -direction towards the $[110]$ -direction of a quantum dot with a radius of 11 nm and height of 2.4 nm. In absence of elongation (top row) there is an intricate dependence of the emission pattern on the orientation of the magnetic field, which is absent when the quantum dot's footprint (green) is compressed in the $[110]$ -direction (bottom row).

591 The situation is more complicated for the Voigt mea-
 592 surements, as it is neither possible to assign the measured
 593 g -factors to a specific carrier, nor to establish their sign:
 594 it is a priori not clear which of the two linearly polarized
 595 Zeeman splittings belongs to which transition. It has
 596 been shown for quantum wells⁴⁸ and ensembles of quan-
 597 tum dots⁴⁹, that the in-plane orientation of the linear
 598 polarisation axis depends on the relative in-plane orienta-
 599 tion of the electron and hole spin. Details of the hole
 600 state, such as light-hole intermixing and the non-linear
 601 remote-band coupling of the magnetic field to the hole
 602 spin, can lead to the peculiar situation where the in-plane
 603 orientation of the polarisation axis depends non-trivially
 604 on the in-plane magnetic field orientation⁴⁹. Only by
 605 measuring this dependence, would it be possible to at-
 606 tribute the Zeeman splittings to a certain carrier.

607 In Fig. 7 we show that this situation also applies to our
 608 quantum dots: we use the $\mathbf{k} \cdot \mathbf{p}$ -model to calculate the

609 in-plane orientation of the linear polarisation axis of the
 610 ground state dipole transitions for various in-plane orienta-
 611 tions of the magnetic field. We note that these effects
 612 are virtually absent when the quantum dot is elongated:
 613 the polarisation axis is relatively unaffected by the in-
 614 plane orientation of the magnetic field. Since we have
 615 no clear experimental evidence for such elongation in our
 616 quantum dots, we pragmatically opted to rely on the si-
 617 multaneous fit of the $\eta = 45^\circ$ and $\eta = 90^\circ$ data, where
 618 the goodness of the fit depends on the assignment of the
 619 Zeeman energies to a certain carrier.

620 The sign of the $g_{e,h}^x$ -factors cannot be determined di-
 621 rectly from the measurements. The inner two peaks of
 622 all quantum dots emitting at energies $\gtrsim 825$ meV are
 623 y -polarized, see for example Fig. 3(a). However, the
 624 inner peaks are x -polarized for quantum dots emitting
 625 $\lesssim 825$ meV, from which we infer that the relative sign
 626 between g_e^x and g_h^x changes. The measured g_e^x -factor is
 627 zero around these energies, see Fig. 4(b). Since we expect
 628 g_e^x to tend to the free electron g -factor of +2 at high emis-
 629 sion energy¹³ (small quantum dots) and to the strained
 630 bulk InAs electron g -factor of about -5 at low emission
 631 energy⁵⁰ (large quantum dots), we choose $g_e^x > 0$ for
 632 emission energies > 825 meV. The sign of g_h^x follows then
 633 automatically.

634 We have found that two of the four peaks below
 635 850 meV in the $\eta = 45^\circ$ measurements dropped signifi-
 636 cantly in intensity. Lacking those two peaks, it was not
 637 possible to separate the electron and hole g -factor for the
 638 Faraday measurements below 850 meV. Using the eigen-
 639 states of the Hamiltonian in Eq. 1, we have calculated
 640 the emission intensity of the peaks for $\eta = 45^\circ$. As the
 641 intensity depends on the g -factors, we used the measured
 642 g -factors to parametrize the intensity as function of the
 643 emission energy. We then find indeed that the emission
 644 intensity of two of the four peaks drops sharply below
 645 850 meV, due to accidental numerical values of the g -
 646 factors. We predict that below 700 meV these two peaks
 647 have sufficient intensity to be measured, though this is
 648 outside the detection range of the InGaAs detector. Note
 649 that the Voigt measurements do span the full detection
 650 range.

651 * j.v.bree@tue.nl

652 † michael.flatte@mailaps.org

653 ¹ D. Loss and D. P. DiVincenzo, Physical Review A **57**, 120
 654 (1998).

655 ² B. E. Kane, Nature **393**, 133 (1998).

656 ³ Y. Kato, R. C. Myers, A. C. Gossard, J. Levy, and D. D.
 657 Awschalom, Science **299**, 1201 (2003).

658 ⁴ J. Pingenot, C. E. Pryor, and M. E. Flatté, Applied
 659 Physics Letters **92**, 222502 (2008).

660 ⁵ T. Andlauer and P. Vogl, Physical Review B **79**, 045307
 661 (2009).

662 ⁶ A. De, C. E. Pryor, and M. E. Flatté, Physical Review

663 Letters **102**, 017603 (2009).

664 ⁷ J. Pingenot, C. E. Pryor, and M. E. Flatté, Physical Re-
 665 view B **84**, 195403 (2011).

666 ⁸ G. Salis, Y. Kato, K. Ensslin, D. C. Driscoll, A. C. Gossard,
 667 and D. D. Awschalom, Nature **414**, 619 (2001).

668 ⁹ R. Hanson, L. P. Kouwenhoven, J. R. Petta, S. Tarucha,
 669 and L. M. K. Vandersypen, Reviews of Modern Physics
 670 **79**, 1217 (2007).

671 ¹⁰ R. J. Warburton, Nature Materials **12**, 483 (2013).

672 ¹¹ J. Houel, J. H. Prechtel, A. V. Kuhlmann, D. Brunner,
 673 C. E. Kuklewicz, B. D. Gerardot, N. G. Stoltz, P. M.
 674 Petroff, and R. J. Warburton, Physical Review Letters

- 675 **112**, 107401 (2014).
676 ¹² A. A. Kiselev, E. L. Ivchenko, and U. Rössler, Phys. Rev.
677 B **58**, 16353 (1998).
678 ¹³ C. E. Pryor and M. E. Flatté, Physical Review Letters **96**,
679 026804 (2006).
680 ¹⁴ C. E. Pryor and M. E. Flatté, Physical Review Letters **99**,
681 179901(E) (2007).
682 ¹⁵ T. Andlauer, R. Morschl, and P. Vogl, Physical Review B
683 **78**, 075317 (2008).
684 ¹⁶ J. van Bree, A. Y. Silov, P. M. Koenraad, M. E. Flatté,
685 and C. E. Pryor, Physical Review B **85**, 165323 (2012).
686 ¹⁷ R. Zielke, F. Maier, and D. Loss, Physical Review B **89**,
687 115438 (2014).
688 ¹⁸ Y. Yafet, Solid State Physics **14**, 2 (1963).
689 ¹⁹ J. van Bree, A. Y. Silov, P. M. Koenraad, and M. E.
690 Flatté, Physical Review Letters **112**, 187201 (2014).
691 ²⁰ J. van Bree, A. Y. Silov, P. M. Koenraad, and M. E.
692 Flatté, Phys. Rev. B **90**, 165306 (2014).
693 ²¹ M. Bayer, G. Ortner, O. Stern, A. Kuther, A. A. Gor-
694 bunov, A. Forchel, P. Hawrylak, S. Fafard, K. Hinzer, T. L.
695 Reinecke, S. N. Walck, J. P. Reithmaier, F. Klopff, and
696 F. Schäfer, Physical Review B **65**, 195315 (2002).
697 ²² T. Nakaoka, T. Saito, J. Tatebayashi, and Y. Arakawa,
698 Phys. Rev. B **70**, 235337 (2004).
699 ²³ D. Kim, W. Sheng, P. J. Poole, D. Dalacu, J. Lefebvre,
700 J. Lapointe, M. E. Reimer, G. C. Aers, and R. L. Williams,
701 Physical Review B **79**, 045310 (2009).
702 ²⁴ N. A. J. M. Kleemans, J. van Bree, M. Bozkurt, P. J.
703 van Veldhoven, P. A. Nouwens, R. Nötzel, A. Y. Silov,
704 P. M. Koenraad, and M. E. Flatté, Physical Review B **79**,
705 045311 (2009).
706 ²⁵ V. Jovanov, T. Eissfeller, S. Kapfinger, E. C. Clark,
707 F. Klotz, M. Bichler, J. G. Keizer, P. M. Koenraad, G. Ab-
708 streiter, and J. J. Finley, Physical Review B **83**, 161303
709 (2011).
710 ²⁶ V. Jovanov, T. Eissfeller, S. Kapfinger, E. C. Clark,
711 F. Klotz, M. Bichler, J. G. Keizer, P. M. Koenraad, M. S.
712 Brandt, G. Abstreiter, and J. J. Finley, Physical Review
713 B **85**, 165433 (2012).
714 ²⁷ M. Bayer, A. Kuther, A. Forchel, A. Gorbunov, V. B. Tim-
715 ofeev, F. Schäfer, J. P. Reithmaier, T. L. Reinecke, and
716 S. N. Walck, Phys. Rev. Lett. **82**, 1748 (1999).
717 ²⁸ A. Högele, M. Kroner, S. Seidl, K. Karrai, M. Atatüre,
718 J. Dreiser, A. Imamoglu, R. J. Warburton, A. Badolato,
719 B. D. Gerardot, and P. M. Petroff, Applied Physics Letters
720 **86**, 221905 (2005).
721 ²⁹ T. Nakaoka, S. Tarucha, and Y. Arakawa, Phys. Rev. B
722 **76**, 041301 (2007).
723 ³⁰ T. Kehoe, M. Ediger, R. T. Phillips, and M. Hopkinson,
724 Review of Scientific Instruments **81**, 013906 (2010).
725 ³¹ B. J. Wittek, R. W. Heeres, U. Perinetti, E. P. A. M.
726 Bakkers, L. P. Kouwenhoven, and V. Zwiller, Physical
727 Review B **84**, 195305 (2011).
728 ³² A. Schwan, B.-M. Meiners, A. Greilich, D. R. Yakovlev,
729 M. Bayer, A. D. B. Maia, A. A. Quivy, and A. B. Hen-
730 riques, Applied Physics Letters **99**, 221914 (2011).
731 ³³ R. S. Deacon, Y. Kanai, S. Takahashi, A. Oiwa,
732 K. Yoshida, K. Shibata, K. Hirakawa, Y. Tokura, and
733 S. Tarucha, Physical Review B **84**, 041302 (2011).
734 ³⁴ T. M. Godden, J. H. Quilter, A. J. Ramsay, Y. Wu, P. Br-
735 ereton, I. J. Luxmoore, J. Puebla, A. M. Fox, and M. S.
736 Skolnick, Physical Review B **85**, 155310 (2012).
737 ³⁵ A. J. Bennett, M. A. Pooley, Y. Cao, N. Sköld, I. Farrer,
738 D. A. Ritchie, and A. J. Shields, Nature Communications
739 **4**, 1522 (2013).
740 ³⁶ J. H. Prechtel, F. Maier, J. Houel, A. V. Kuhlmann,
741 A. Ludwig, A. D. Wieck, D. Loss, and R. J. Warburton,
742 Phys. Rev. B **91**, 165304 (2015).
743 ³⁷ S. Takahashi, R. S. Deacon, A. Oiwa, K. Shibata, K. Hi-
744 rakawa, and S. Tarucha, Physical Review B **87**, 161302
745 (2013).
746 ³⁸ C. Pryor, Physical Review B **57**, 7190 (1998).
747 ³⁹ K. Gündoğdu, K. C. Hall, E. J. Koerperick, C. E. Pryor,
748 M. E. Flatté, T. F. Boggess, O. B. Shchekin, and D. G.
749 Deppe, Appl. Phys. Lett. **86**, 113111 (2005).
750 ⁴⁰ M. Montazeri, M. Fickenscher, L. M. Smith, H. E. Jackson,
751 J. Yarrison-Rice, J. H. Kang, Q. Gao, H. H. Tan, C. Ja-
752 gadish, Y. Guo, J. Zou, M.-E. Pistol, and C. E. Pryor,
753 Nano Letters **10**, 880 (2010).
754 ⁴¹ I. Vurgaftman, J. R. Meyer, and L. R. Ram-Mohan, Jour-
755 nal of Applied Physics **89**, 5815 (2001).
756 ⁴² D. Gammon, A. Efros, J. Tischler, A. Bracker, V. Korenev,
757 and I. Merkulov, in *Quantum Coherence Correlation and*
758 *Decoherence in Semiconductor Nanostructures*, edited by
759 T. Takagahara (Academic Press, San Diego, 2003) pp. 207
760 – 280.
761 ⁴³ H. W. van Kesteren, E. C. Cosman, W. A. J. A. van der
762 Poel, and C. T. Foxon, Phys. Rev. B **41**, 5283 (1990).
763 ⁴⁴ V. V. Belykh, A. Greilich, D. R. Yakovlev, M. Yacob, J. P.
764 Reithmaier, M. Benyoucef, and M. Bayer, Phys. Rev. B
765 **92**, 165307 (2015).
766 ⁴⁵ R. Winkler, *Spin-orbit Coupling Effects in Two-*
767 *Dimensional Electron and Hole Systems* (Springer,
768 Berlin, 2003).
769 ⁴⁶ T. B. Bahder, Physical Review B **41**, 11992 (1990).
770 ⁴⁷ F. V. Kyrychenko and J. Kossut, Physical Review B **70**,
771 205317 (2004).
772 ⁴⁸ Y. G. Kusrayev, A. V. Koudinov, I. G. Aksyanov, B. P. Za-
773 kharchenya, T. Wojtowicz, G. Karczewski, and J. Kossut,
774 Physical Review Letters **82**, 3176 (1999).
775 ⁴⁹ T. Kiessling, A. V. Platonov, G. V. Astakhov, T. Slobod-
776 skyy, S. Mahapatra, W. Ossau, G. Schmidt, K. Brunner,
777 and L. W. Molenkamp, Physical Review B **74**, 041301
778 (2006).
779 ⁵⁰ G. Hendorfer and J. Schneider, Semiconductor Science and
780 Technology **6**, 595 (1991).